

## Energy confinement and pellet fuelling in MAST

M. Valovič, R. Akers, M de Bock, L. Garzotti, C. Gurl, C. Michael, G. Naylor, A. Patel, R. Scannell, M. Wisse, W. Guttenfelder<sup>1</sup>, J. Candy<sup>2</sup>, J. Páleník<sup>3</sup> and the MAST team

EURATOM/CCFE Fusion Association, Culham Science Centre, Abingdon, OX14 3DB, UK  
<sup>1</sup>PPPL, Princeton, USA; <sup>2</sup>General Atomics, USA; <sup>3</sup>Association EURATOM Comenius University, Slovakia;  
 email: martin.valovic@ccfe.ac.uk

**Abstract.** A factor of 4 dimensionless collisionality scan of H-mode plasmas in MAST shows that the thermal energy confinement time scales as  $B\tau_{Eth} \propto \nu_*^{-0.82 \pm 0.1}$ . Local heat transport is dominated by electrons and is consistent with global scaling. Neutron rate is in a good agreement with  $\nu_*$  dependence of  $\tau_{Eth}$ . The gyrokinetic code GYRO indicates that micro-tearing turbulence might be a possible candidate for such trend. A factor of 1.4 dimensionless safety factor scan shows that the energy confinement time scales as  $B\tau_{Eth} \propto q_{eng}^{-0.85}$ . Scalings rely on validation of anomalous fast ion losses.

Particle transport and fuelling is studied using high field side pellet deposition into NBI heated H-mode plasmas. High spatial resolution ( $\sim 1.5$ mm) of visible bremsstrahlung imaging of the pellet trajectory reveals discrete structures (striations). The wavelength of the striations is in the range of  $\sim 4 - 30$  mm, close to ion Larmor radius, with possible indication of correlation with bremsstrahlung emission amplitude. Pellet fuelling is favourable for H-mode access when compared to gas puffing.

### 1. Introduction

First applications of spherical tokamaks (ST) are foreseen as intense fusion volume neutron sources. Example of such a device is the Component Test Facility based on Spherical tokamak (ST-CTF) [1] and the relevance of such source to fusion energy programme was noted in [2]. So far the extrapolations to ST-CTF were done using IPB98y2 confinement scaling derived from conventional tokamaks [3]. This scaling is however not in line with MAST [4] and NSTX [5] data, in particular spherical tokamaks display stronger dependence of energy confinement on toroidal magnetic field and weaker dependence on plasma current. In this paper we further refine scalings of heat transport using dimensionless scans along normalised collisionality and safety factor.

Second part of the paper reports on latest results on pellet fuelling in MAST. Pellets are so far the only realistic choice for fuelling in ITER, DEMO, and likely ST-CTF and its efficiency is critical for minimising tritium throughput [6] and inventory. Growing desire for increased pumping, ELM mitigation or expanding the divertor volume further strengthen the need for understanding and calibration of pellet fuelling models.

### 2. Gap analysis

At present MAST H-mode confinement dataset spans the following space of engineering parameters: plasma current  $I_p = (0.59 - 1.13)MA$ , major radius at geometric axis  $R = (0.77 - 0.88)m$ , minor radius  $a = (0.50 - 0.62)m$ , elongation  $\kappa = 1.6 - 2.1$ , triangularity  $\delta = 0.3 - 0.5$ , vacuum toroidal field at the geometric radius  $B = (0.34 - 0.50)T$  and line averaged density  $\bar{n}_e = (2.1 - 5.1) \times 10^{19} m^{-3}$ . Total injected NBI power is  $P_{NBI} < 3.5MW$  and the energy of neutral beams is  $E < 65keV$ . Beams are injected in the direction of plasma current. In our studies plasmas have double null divertor configuration with deuterium as a working gas. Sawteeth are generally avoided by an application of neutral beam heating (NBI) during current ramp-up.

To analyse the gap between existing MAST data and future ST-CTF device the dataset is mapped to the space of main volume averaged dimensionless parameters such as toroidal  $\beta$ , normalised Larmor radius  $\rho_* = (MT)^{1/2} / (aB)$ , engineering safety factor  $q_{eng} =$

$2\pi a^2 \kappa B / (R \mu_0 I_p)$  and normalised collisionality  $\nu_{*q} \propto \bar{n}_e T^{-2} R q_{eng} (R/a)^{3/2}$ . Here  $T = W_{th} / (3V \bar{n}_e)$  is the volume averaged temperature,  $M$  is the ion mass and  $V$  is the plasma volume,  $W_{th}$  is the thermal energy content. Inspection of data shows that the largest extrapolation gap between MAST data and ST-CTF device is along the normalised collisionality. This gap is about one and half orders of magnitude large and thus even small error in the scaling of energy confinement time with collisionality means large prediction error. Along the safety factor, there is no large gap between MAST and ST-CTF, however, only plasmas with  $I_p > 1MA$  have  $q_{eng}$  as predicted for ST-CTF. These high current plasmas have, however, control difficulties such as low ELM frequency and high power for non-inductive operation. Thus it seems to be desirable to increase  $q_{eng}$  in ST-CTF operation point. Whether such a change is possible will depend on the scaling of confinement on safety factor.

To determine aforementioned scalings let us write the thermal energy confinement time in a conventional power law form:

$$\tau_{E,th} B \propto \rho_*^{x_\rho} \beta^{x_\beta} q_{eng}^{x_q} \nu_*^{x_\nu}. \quad (1)$$

Here plasma shape is assumed to be the same. Collisionality is defined as  $\nu_* \propto \bar{n}_e T^{-2} R$  so that the safety factor dependence is explicit.

### 3. Collisionality scan of energy transport

The exponent  $x_\nu$  in scaling formula (1) can be determined from a set of plasmas which differ in collisionality  $\nu_*$  but other dimensionless parameters are kept constant. From the requirement that  $\rho_* \propto \sqrt{T}/B = const$ ,  $\beta \propto \bar{n}_e T / B^2 = const$ ,  $q \propto B / I_p = const$  one finds that the plasma density, temperature and plasma current should depend on toroidal magnetic field as:  $\bar{n}_e \propto B^0$ ,  $T \propto B^2$  and  $I_p \propto B$ . The breadth of the scan is controlled by a span of toroidal magnetic field as  $\nu_* \propto n / T^2 \propto B^{-4}$ . In MAST, for fixed major radius of  $R = 0.81m$  the maximum toroidal field is  $B_{max} = 0.50T$ . The lower point was set empirically to  $B_{min} = 0.34T$  so that the beam deposition is not significantly affected by unconfined orbits. Such a choice provides the collisionality scan by a factor of  $(B_{max}/B_{min})^4 = 4.6$ .

**3.1 Matching dimensionless parameters.** Table 1 shows the parameters of 2 discharges that has been arranged to approach the requirements for collisionality scan. The first parameter to match is the plasma density. Due to the dependence of L-H threshold on magnetic field the plasma with lower  $B$  enters H-mode at lower density than its higher field counterpart. Therefore to match the density the time slice for high  $B$  plasma has to be selected at the beginning of H-mode phase where the contribution of change of energy content to power balance is substantial. Table 1 shows that the line averaged density has been matched within  $\pm 1.5\%$ . The density profiles are flat as it is typical for ELMy H-mode and the quality of matching of profiles is shown in figure 1a.

Table 1.

Shot number	22769	22664
Time [s]	0.20	0.23
$a$ [m]	0.57	0.58
$R$ [m]	0.813	0.816
$\kappa$	2.0	2.0
$\delta$	0.42	0.45
$B$ [T]	0.34	0.50
$I_p$ [kA]	592	886
$\bar{n}_e$ [ $10^{19} m^{-3}$ ]	3.2	3.3
$q_{eng}$	2.3	2.3
$W_{th}$ [kJ]	41	87
$W_e$ [kJ]	20	40
$P_{NBI}$ [MW]	3.0	3.2

The second parameter to adjust is the plasma temperature. In control room this is done by varying the neutral beam power. Table 1 shows that the ratio of thermal energy content  $W_{th}$  along the scan is 2.07, in good agreement to required value of  $(B_{max}/B_{min})^2 = 2.16$ . Such match is achieved by 10% difference in beam power. Here,  $W_{th}$  is calculated from the electron density  $n_e$  and electron temperature  $T_e$  measured by Thomson scattering, ion temperature  $T_i$  measured by charge exchange resonant spectroscopy (CXRS) and plasma shape from

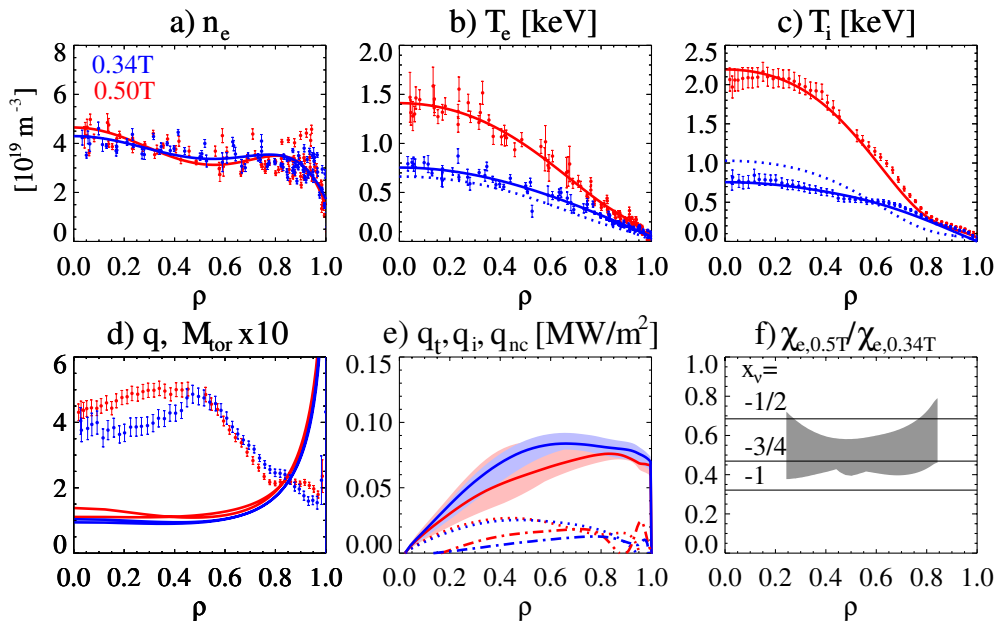


Figure 1. Profiles in collisionality scan in table 1 (#22769 – blue symbols, #22664–red symbols). (a) electron density  $n_e$ , (b): electron temperature  $T_e$ . (c) ion temperature  $T_i$ . (d) discrete symbols: toroidal Mach number  $M_{tor} = V_{tor} / (T_i / m_i)^{1/2}$ , solid lines:  $q$  profiles. (e) solid lines: total heat flux  $q_t$ , dotted lines: ion heat flux  $q_i$ , dash-dot lines: ion neoclassical heat flux  $q_{nc}$ . (f) shaded area: ratio of electron heat diffusivities  $\chi_{e,0.5T} / \chi_{e,0.34T}$ , lines the ratios expected from different exponents.  $\rho = \psi_N^{0.5}$ , where  $\psi_N$  is the normalised poloidal magnetic flux.

equilibrium reconstruction (EFIT) constrained by motional Stark effect (MSE). Effective charge  $Z_{eff}$  is measured by bremsstrahlung emission and except plasma edge is close to 1.

Table 1 shows that the ratio of electron to ion temperatures is not exactly constant along the scan. Variation of electron energy content  $W_e$  along the scan is 2.0 while the variation of ion energy content  $W_i = W_{th} - W_e$  is 2.2. In other words electron temperature varies somewhat less than required for ideal scan while ion temperature varies more than required. This is also seen on electron and ion temperature profiles shown in figure 1b and 1c where dotted line represents the perfect match. The shape of  $T_e$  profile is preserved along the scan but the profile of  $T_i$  becomes more peaked at lower collisionality. In order to keep the  $T_i/T_e$  ratio constant along the scan a separate heating system would be required and this is not yet available on MAST. As a result of changing  $T_i/T_e$  along the scan the breadth of  $\nu_*$  scan depends on which temperature is used in the definition of volume averaged collisionality. The collisionality defined from electron temperature  $\nu_{*e} \propto \bar{n}_e^3 / W_e^2$  varies by a factor of 3.6, while  $\nu_* \propto \bar{n}_e^3 / W_{th}^2$  varies by a factor of 4.1.

The mismatch of electron toroidal beta and normalised Larmor radius measured by volume averaged electron temperature, are within ten percents:  $\beta_{e,0.5T} / \beta_{e,0.34T} = 0.92$  and  $\rho_{*e,0.5T} / \rho_{*e,0.34T} = 0.96$ . In tokamaks the  $\beta$  dependence is typically bounded by the exponent in the range of  $x_\beta \in (-1, 0)$  while the  $\rho_*$  dependence is typically described by gyro-Bohm scaling with  $x_\rho \approx -3$ . Therefore the mismatch in  $\rho_*$  is more significant. The error on  $\nu_*$  exponent due to  $\rho_*$  mismatch is  $\delta x_{\nu_*} = 3 \ln(\rho_{*e,0.5T} / \rho_{*e,0.34T}) / \ln(\nu_{*e,0.5T} / \nu_{*e,0.34T}) = 0.1$ , and its direction is such that it makes the  $x_{\nu_*}$  exponent less negative.

Profiles of safety factor  $q$  are well matched for the pair, however, high  $\nu_*$  shot has  $q < 1$  in the plasma centre and this plasma is sawtoothed. Toroidal Mach number  $M_{tor}$  is similar for both shots.

3.2 *Validation of power loss.* When dimensionless parameters are matched the collisionality exponent is determined by the change of thermal power loss  $P_{L,th}$  along the scan:  $P_{L,th} \propto \nu_*^{-x_\nu - 3/4}$ . The thermal power loss  $P_{L,th}$  is calculated by the TRANSP code [7] with the help of the MC3 data pre-processor. Number of test particles in Monte-Carlo simulations of beam ions varied between  $10^3$  to  $10^4$  with no significant difference on calculated heating power. Better convergence is sometimes observed when more test particles is used, probably due to reduced numerical noise. Special attention has to be paid to the distribution of power between full, half and third energy components because the beam power was adjusted mainly by beam current while the changes in beam voltage were smaller. Energy components are calculated from actual beam perveance using calibration tables. Without corrections the neutron emission calculated by TRANSP is higher than the values measured by fission chamber. Simultaneously the fast ion energy content calculated by TRANSP is larger than found by EFIT constrained by MSE. These differences are attributed to the anomalous loss of fast ions. Good agreement between calculated and measured neutron rate is found with fast ion diffusion coefficient  $D_{fast} = 2\text{m}^2/\text{s}$  and  $3\text{m}^2/\text{s}$  for low and high  $\nu_*$  respectively. Such values of  $D_{fast}$  result in approximately the same total heat flux  $q_t$  for both shots in the scan as seen in figure 1e. This is reflected also in global power loss that is similar for both shots  $P_{L,th,0.34T} / P_{L,th,0.50T} = 1.05$ . Such a value gives the collisionality exponent of  $x_\nu = -\ln(P_{L,th,0.34T} / P_{L,th,0.50T}) / \ln(\nu_{*0.34T} / \nu_{*0.50T}) - 3/4 = -0.79$ .

Figure 1e shows that most of the total heat flux  $q_t$  flows along electrons while ion heat flux is close to neoclassical level. For this reason only electron heat flux was analysed in detail. Figure 1f shows that the ratio of electron heat diffusivities along the scan can be bracketed by collisionality dependence of  $\chi_e B^{-1} \propto \nu_{*e}^{1/2 \text{ to } 1}$ . This is in a good agreement with the global energy confinement time.

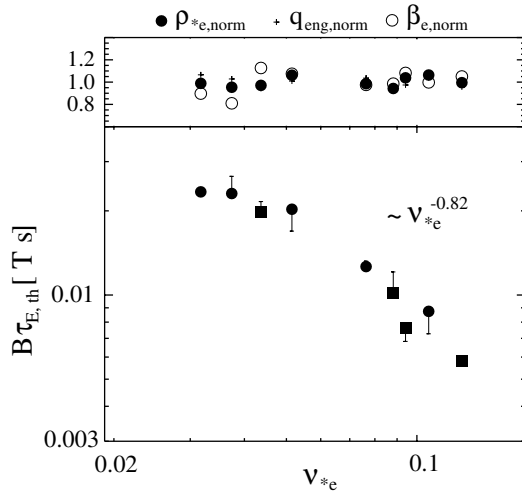


Figure 2. Main panel: collisionality scan of thermal energy confinement time. Vertical bar is the size of  $\rho_{*e}$  correction assuming gyro Bohm scaling. Circles: shape as in table 1, squares: shape with  $R = 0.86\text{m}$ ,  $\kappa = 1.7$ . Top panel: variations of electron Larmor radius, beta and  $q_{eng}$ , all normalised to average values along the scan. Here  $\nu_{*e} \propto \bar{n}_e \langle T_e \rangle^{-2} R$ ,  $\langle T_e \rangle = \frac{2}{3} W_e / (V \bar{n}_e)$ .

Robustness of the scaling from two point scan has been tested by adding more data points. The results is a dataset with larger span along the collisionality while variations of  $\rho_{*e}$ ,

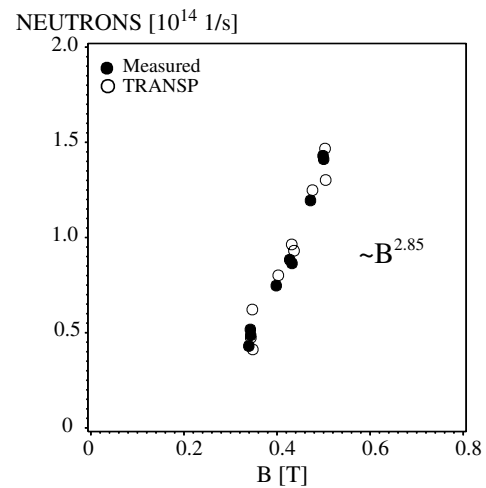


Figure 3. Toroidal field dependence of neutron rate for dataset in figure 2. The fit is evaluated only on measured neutron data.

$\beta_T$  and  $q_{eng}$  are kept within 20% as shown in figure 2, top panel. Log-linear regression of the extended dataset of plasma with shapes similar to that in table 1 provides the scaling of  $\tau_{E,th} B \propto \nu_*^{-0.82}$ , i. e. similar to two point scan result. Data with lower elongation show similar trend (figure 2).

Validation procedure described above can be checked by dependence of D-D fusion neutron rate  $S_{DD}$  on toroidal magnetic field. Log-linear regression for extended dataset gives  $S_{DD} \propto B^{2.85}$  as seen in figure 3. In the dataset the standard deviation of beam voltage is small, 3.8%, and  $Z_{eff}$  in the centre is close to 1. Therefore the neutron rate, dominated by beam-thermal reactions, is  $S_{DD} \propto \tau_{sd} P_{NBI,heat}$  where  $\tau_{sd}$  is the beam slowing down time and  $P_{NBI,heat}$  is the dissipated beam power. Ignoring ohmic power and  $dW_{th}/dt$  the neutron rate scales with magnetic field as  $S_{DD} \propto T_e^{3/2} P_{L,th} \propto T_e^{3/2} \nu_*^{-x_\nu - 3/4} \propto B^{4x_\nu + 6}$ . Comparing this with measured trend one finds that the collisionality exponent is  $x_\nu = -0.79$ , in good agreement with previous analysis.

**3.3 MAST Upgrade.** Planned increase of magnetic field by a factor of 1.5 will theoretically allow to extend the above scan by a factor of  $1.5^4 = 5$  towards the lower  $\nu_*$  values. For such a plasma  $I_p = 1.3MA$  and the central electron temperature should be  $T_{e,0} = T_{e,0}(\#22664) \times 1.5^2 = 3keV$ . Let us assume that MAST-U will follow the trend observed in other tokamaks so that with decreasing  $\nu_*$  the scaling becomes weaker, say as  $x_\nu = -1/3$  [8]. Then the power required to reach such electron temperature has to be by a factor of  $P_{L,th} \propto \nu_*^{-x_\nu - 3/4} = (1/5)^{1/3 - 3/4} \sim 2$  larger than for scan in table 1. Note that even  $x_\nu = -1/3$  represents stronger  $\nu_*$  dependence than in IPB98y2 scaling where  $x_\nu = 0$ .

#### 4. Interpretation of $\nu_*$ scan

GYRO code [9] has been used to assist the  $\nu_*$  scan. Experimental profiles from high  $\nu_*$  plasma in figure 1 have been used in the code as a starting point and then the collisionality has been varied numerically. Analysis shows that the linear growth rates  $\gamma$  of ITG, ETG and TEM modes do not exhibit collisionality dependence which could be linked to the experimental data i.e. decreasing  $\gamma$  with decreasing  $\nu_*$ . Only micro-tearing modes display such behaviour as shown in figure 4. It is seen that normalised  $\gamma$  indeed decreases as collisionality is reduced. Nevertheless this dependence seems to be quite weak in order to explain the diffusivity scaling by mixing length estimate. Collisionality could also affect the transport through the stabilisation of turbulence via plasma rotation. However, as the Mach number is preserved along the  $\nu_*$  scan (figure 1d) this would require that the growth rates deviate from usual sound speed scaling  $\gamma \propto c_s/a$ . Collisionality dependence could also arise from fully developed turbulence and/or from accumulated mismatch of other sensitive parameters such as temperature gradients. Another candidate is a combination of profile stiffness and  $\nu_*$  dependence of transport at plasma edge. Future work is planned to explore these hypotheses.

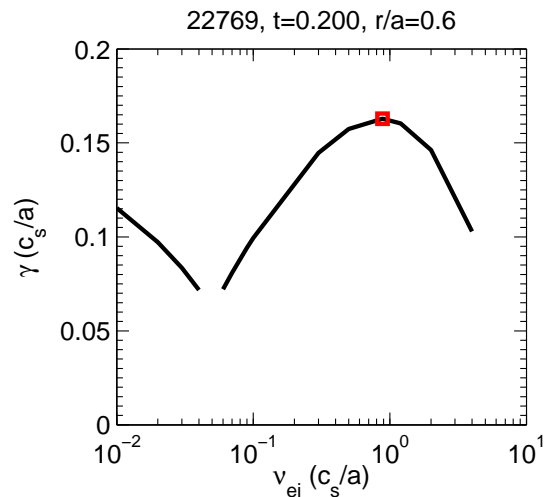


Figure 4. Linear growth rate of micro-tearing modes calculated by GYRO code. Red symbol represents the high  $\nu_*$  point in table 1.

### 5. q-scan

Safety factor exponent  $x_q$  in the scaling (1) has been evaluated using factor of 1.46 scan of plasma current at constant toroidal magnetic field, electron density and plasma temperature. Figure 5 shows the profile analysis for 2 plasmas from such a scan. Plasma densities and temperatures are well matched in the pair (Figure 5a-c). The match of thermal energy content is also excellent:  $W_{th} = 69.8 - 69.9 kJ$ . Small variations of plasma geometry outside our control means that  $q_{eng}$  varies by a factor of 1.32, i.e. lower than the ratio of  $I_p$  (figure 5d). In order to match the plasma temperature the heating power has to be adjusted so that higher power is needed for lower  $I_p$ . The exponent of safety factor in the scaling (1) is then related to the thermal power loss as  $P_{L,th} = W_{th}/\tau_{E,th} \propto q_{eng}^{-x_q}$ . TRANSP analysis shows that for low  $I_p$  (high power) anomalous fast ion losses with diffusivity of  $D_{fast} = (0.5 - 1) m^2/s$  are needed to match the measured neutron rate. For high  $I_p$  (low power)  $D_{fast} = (0 - 0.5) m^2/s$  is sufficient. TRANSP analysis gives for ratio of thermal power loss  $P_{th,0.9MA}/P_{th,0.6MA} = 0.81$  and consequently the safety factor exponent is  $x_q = -0.73$ . This is also confirmed by local heat transport analysis. Figures 5e and 5f show that the ratio of heat flux  $q_t$  is consistent with the value of  $x_q$  in global confinement time scaling. Similarly as in collisionality scan most of the heat is transported along electron channel (figure 5e). The ratio of electron heat diffusivities in the outer half of the plasma  $\rho \in (0.5, 0.9)$  is in the range of  $\chi_{e,0.9MA}/\chi_{e,0.6MA} \in (0.6, 0.9)$  while the ratio of local values of safety factor  $q_{0.9MA}/q_{0.6MA} \in (0.75, 0.95)$ . This would again broadly imply linear scaling of  $\chi_e$  with  $q$ , however, the radial profiles are more complicated to be described by  $\chi_e \propto q^{-x_q}$  with a single value of  $x_q$  (see figure 5f).

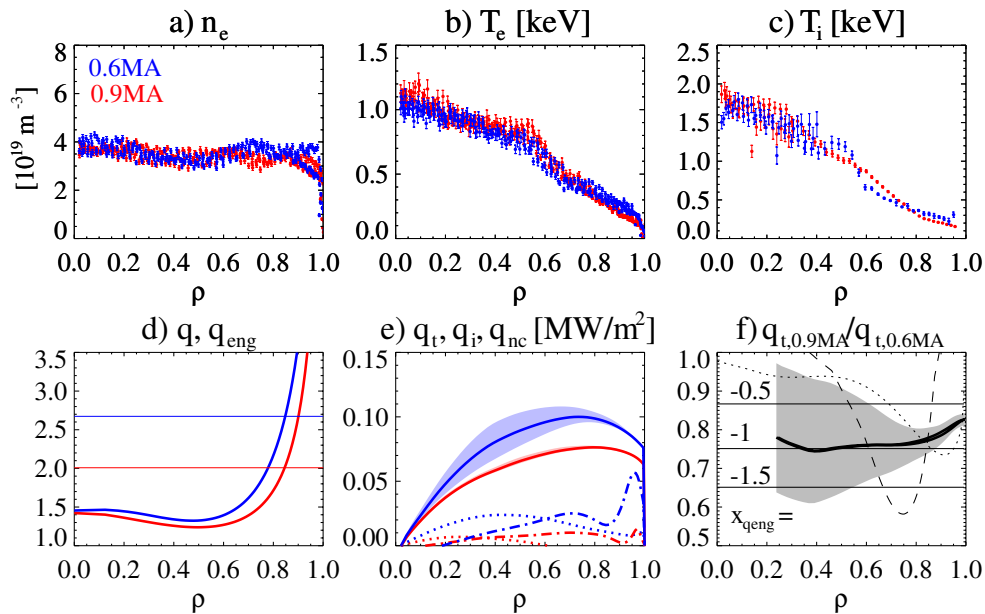


Figure 5. Profiles in  $q$  scan. Blue symbols: #24206,  $I_p = 0.62MA$ ,  $P_{INJ} = 3.49MW$ . Red symbols #24207,  $I_p = 0.91MA$ ,  $P_{INJ} = 1.78MW$ . Other notations as in figure 1. (f) solid line:  $q_{t,0.9MA}/q_{t,0.6MA}$  dashed line:  $\chi_{e,0.9MA}/\chi_{e,0.6MA}$ , dotted line:  $q_{0.9MA}/q_{0.6MA}$ .

Robustness of the scaling has been checked on the dataset of 6 observations, each representing one discharge. Top panel in figure 6 shows that the line averaged density, electron and thermal energy contents are constant along the safety factor scan. Main panel in figure 6 shows the values thermal energy confinement time calculated by TRANSP. Log-linear regression on the dataset gives the scaling of  $B\tau_{E,th} \propto q_{eng}^{-0.85}$ , consistent with 2 point scan

above. Such dependence is weaker than in IPB98y2 scaling where  $B\tau_{E,th} \propto q_{eng}^{-3}$ , and is closer to data from DIII-D where the exponent  $x_q \in (-2.4, -1.4)$  [10].

Finally note that dimensionless scalings with  $q_{eng}$  combined with  $v_*$  scaling are consistent with the dependence of  $\tau_{E,th}$  on  $I_p$  and  $B$  assuming gyro-Bohm transport as discussed in our previous paper [4].

## 6. Effect of fast ion losses

Both scalings rely on a simple model of anomalous fast ion losses that are described by a spatial diffusion coefficient  $D_{fast}$ , which is constant along the minor radius and is energy independent. The value  $D_{fast}$  is set to match the calculated neutron rate to a measured value. The larger  $D_{fast}$  the smaller the thermal power loss  $P_{th}$  and larger the  $\tau_{E,th}$ . For  $v_*$  scan (table 1) inclusion of fast ion losses decreases the power loss by a factor of 1.4. This correction is however the same for both low and high  $v_*$  points so that the ratio  $P_{th,0.34T} / P_{th,0.5MA}$  remains unchanged (within 3%) and the exponent  $x_v$  is unaffected.

For  $q$  scan, fast ion losses are needed only for high  $q$  data while for low  $q$  the neutron rate is well matched without or small fast ion diffusion. This asymmetry means that inclusion of fast ion losses makes the safety factor scaling weaker. In 2 point scan (figure 5) ignoring fast ion losses changes  $P_{th,0.9MA} / P_{th,0.6MA}$  from 0.81 to 0.69 and consequently the safety factor scaling becomes stronger with  $x_q = -1.32$ . If our fast ion model is incorrect and for example reduced neutron rate is due to the enhanced diffusion in velocity space or due to the very localised spatial diffusion in the core, then the power is not lost. In that case the corrections described above has to be revisited.

## 7. Pellet fuelling

**7.1 Striations.** Fuelling is studied on MAST using pellets (diameter  $\sim 1$ mm, velocity  $\sim 400$ m/s) launched from vertical/high field side into NBI heated H-mode plasmas. Re-deposition of pellet particles by  $\nabla B$  drift of discrete plasmoids is a critical mechanism for ITER fuelling. Plasmoids are linked to striations observed in open shutter visible bremsstrahlung imaging of pellet track (spatial resolution 1.5mm). Figure 7 shows the spatial separation  $\Delta z$  of individual striations in the direction of pellet trajectory as obtained from bremsstrahlung images. The dataset indicates positive correlation of  $\Delta z$  with the intensity of the emission of individual striation with correlation coefficient  $r = 0.57$ . Because emission intensity increases as pellet evaporates deeper into the plasma this also means that striation separation  $\Delta z$  increases with increasing ambient plasma temperature  $T_{e,\infty}$ . This however would be in contrast with the most accepted model of striation formation based on  $E \times B$  driven magnetic interchange instability of plasmoids detaching from the pellet [11]. In this model the linear growth rate of instability is  $\gamma_{E \times B} \propto T_{e,\infty} / B$  giving inverse temperature dependence for  $\Delta z = v_{pel} / \gamma_{E \times B} \propto 1 / T_{e,\infty}$ . Second interesting observation is that striation separation, both measured and predicted by  $E \times B$  driven instability, are comparable to Larmor radius  $\rho_s \propto (2T_e M)^{1/2} / B$  (figure 7). This

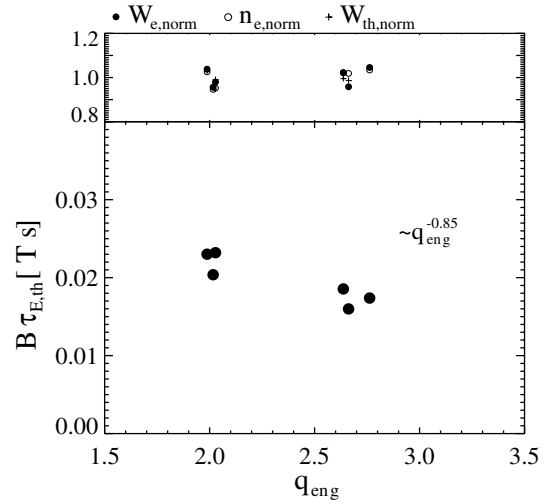


Figure 6. Main panel: safety factor scan of thermal energy confinement time. Top panel: variations of electron energy content, line average density and thermal energy, all normalised to average values along the scan.

indicates that finite Larmor radius effects might be important for plasmoid dynamics. Pellet-triggered Thomson scattering data are being analysed to test further the plasmoid models.

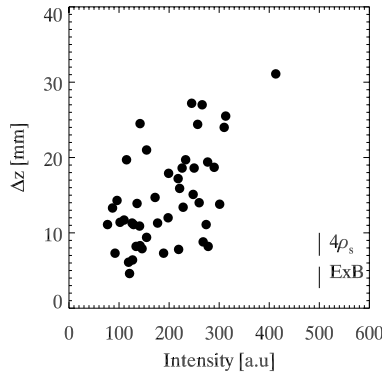


Figure 7 (above). Striation separation  $\Delta z$  plotted against intensity of bremsstrahlung emission.

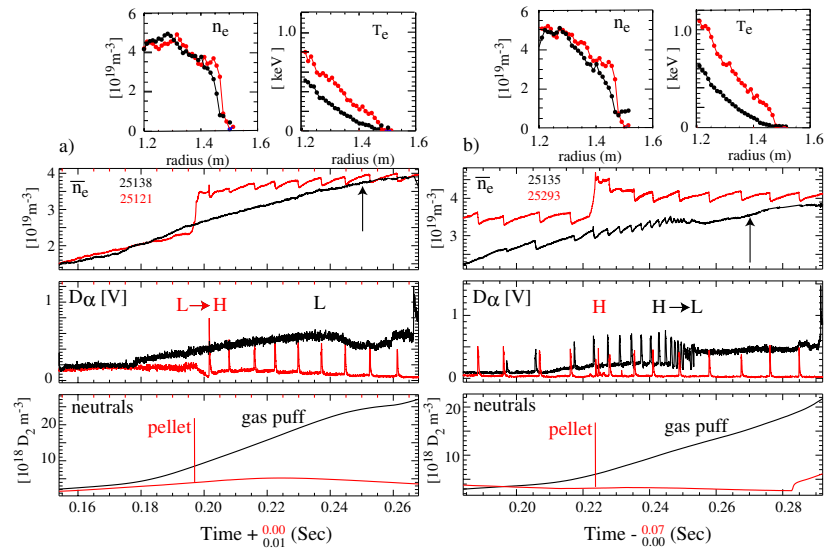


Figure 8 (right). Effect of fuelling method on L-H (a) and H-L (b) transition. High field side pellet (red) and low field side gas puff (black) is used.  $P_{\text{NBI}}=3.2\text{MW}$ , shots 25138, 25121, 25135:  $I_p=0.74\text{MA}$ ,  $B=0.40\text{T}$ ; shot 25293:  $I_p=0.85\text{MA}$ ,  $B=0.47\text{T}$ . Top panels show edge electron density and temperature profiles at times indicated by arrows. Note time offsets for shots 25138, 25293.

**7.2 H-mode threshold with pellets.** Application of pellet fuelling instead of gas puffing provides a clear example of decoupling from conventional H-mode power threshold formulas which use the line averaged density as a control variable:  $P_{th} = F(\bar{n}_e)$ . Figure 8a shows that raising the plasma density by pellet results in a transition into H-mode while with gas puffing the plasma stays in L-mode despite the same line average density. Similarly the favourable effect of pellet fuelling is seen when the density is increased during H-mode: With pellet plasma remains in H-mode while gas puffing causes transition to L-mode as shown in figure 8b. In both cases the pellet fuelled H-mode and gas fuelled L-mode have similar edge density as seen on top panels in figure 8. However the H-mode plasmas show somewhat steeper edge density gradient and significantly higher edge electron temperature. This example shows how method of fuelling can be one of the variables controlling the H-mode access.

*This work was funded by the RCUK Energy Programme under grant EP/G003955 and the European Communities under the contract of Association between EURATOM and CCFE. The views and opinions expressed herein do not necessarily reflect those of the European Commission.*

- [1] VOSS, G, et al., 2007, Fusion Eng. Des. doi :10.10016/j.fusengdes.2008.05.002
- [2] European Commission. "R&D Needs and Required Facilities for the Development of Fusion as an Energy Source" October 2008, [http://ec.europa.eu/research/energy/pdf/978-92-79-10057-4\\_en.pdf](http://ec.europa.eu/research/energy/pdf/978-92-79-10057-4_en.pdf)
- [3] ITER Physics Basis, Nucl. Fusion **39** (1999) 2175
- [4] VALOVIĆ, M. et al., Nucl. Fusion **49** (2009) 075016
- [5] KAYE, S. et al., Nucl. Fusion **47** (2007) 499
- [6] VALOVIĆ, M. et al., Nucl. Fusion **48** (2008) 075006
- [7] TRANSP code, <http://w3.pppl.gov/transp/>
- [8] PETTY, C.C., Phys. Plasmas **15** (2008) 080501
- [9] WALTZ, R.E., CANDY, J., ROSENBLUTH, M.N., Phys. Plasmas **9** (2002) 1938.
- [10] PETTY, C.C. et al., Phys. Plasmas **5** (1998) 1695
- [11] PARKS, P. B. et al, Phys. Plasmas **7** (2000) 1968